

NATIONAL ADVISORY COMMITTEE FOR AERONAUTICS

TECHNICAL NOTE 3672

INVESTIGATION AT HIGH SUBSONIC SPEEDS OF A
BODY-CONTOURING METHOD FOR ALLEVIATING
THE ADVERSE INTERFERENCE AT THE ROOT
OF A SWEPTBACK WING

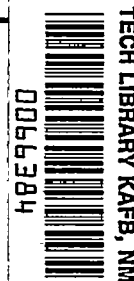
By John B. McDevitt and William M. Haire

Ames Aeronautical Laboratory
Moffett Field, Calif.



Washington
April 1956

AFMDC
TECHNICAL LIBRARY
1 201





NATIONAL ADVISORY COMMITTEE FOR AERONAUTICS

TECHNICAL NOTE 3672

INVESTIGATION AT HIGH SUBSONIC SPEEDS OF A
BODY-CONTOURING METHOD FOR ALLEVIATING
THE ADVERSE INTERFERENCE AT THE ROOT
OF A SWEEPBACK WING¹

By John B. McDevitt and William M. Haire

SUMMARY

A body-contouring method for alleviating at subsonic speeds the adverse interference at the root of a high-aspect-ratio sweptback wing was investigated. Several bodies used in combination with a 35° sweptback wing were modified, as proposed by Küchemann, by shaping the body so as to counteract the distorting velocities at the wing-body junction.

Although modifying the body shape did not significantly affect the aerodynamic characteristics at subcritical speeds, beneficial results were obtained at free-stream Mach numbers above the critical. Improved aerodynamic characteristics were evidenced by large reductions of drag, an increase in lift-curve slope, and a reduced change of pitching-moment-curve slope with increasing Mach number.

Additional tests, which involved changes in wing position relative to the body, indicated that wing position had little effect on the aerodynamic characteristics of the unmodified wing-body combinations.

INTRODUCTION

The effect of sweep for delaying the onset of compressibility drag has generally been somewhat less beneficial than indicated by simple-sweep theory. This is caused, at least in part, by an adverse velocity distribution at the root of the swept wing. The subsonic wing theories of references 1 and 2 indicate that the velocity distribution at the root of a swept wing is, because of reflection at the plane of symmetry, distorted in such a manner that the chordwise position of maximum velocity

¹Supersedes NACA RM A54A22 by John B. McDevitt and William M. Haire, 1954.

is displaced rearward. Furthermore, the maximum velocity at the root of the swept wing may be considerably higher than that for an infinite yawed wing and, consequently, the premature formation of strong local shocks in the vicinity of the root can be expected.

The velocity distortion can be alleviated by altering either the wing geometry near the root or by contouring the body in the vicinity of the wing-body junction. Shaping the sides of the body to conform to the general shape of a streamline on a yawed wing has been suggested in reference 3. Experimental investigations described in references 4 and 5 were based on this method and some beneficial results were obtained. A modified swept-wing-root profile was also investigated in the research reported in reference 4.

The design of wing-fuselage junctions for subsonic speeds has been given an exhaustive treatment by Küchemann (refs. 6 and 7). In one of the methods proposed by Küchemann, the body is represented by a cylinder on which ring vortices are distributed so that the induced axial component of velocity cancels the swept-wing interference velocity. By integration of the induced lateral velocity, the radial modification necessary to shape the wing-body junction is determined. For further details concerning the use of ring vortices see reference 8.

The present report gives the results of an experimental investigation of this method at high subsonic speeds. A summary of the theoretical method for determining the required body modifications and a detailed description of the application of this method as used in the present investigation are presented in the Appendix of this report. Although the present investigation was conducted primarily to evaluate a particular body contouring method, several related studies were conducted. In order to obtain information concerning the effect of the swept-wing position relative to the body on the aerodynamic characteristics, a body was tested with the wing in forward and in rearward positions. A body was also tested with the wing at the center line of the body and in a raised position. Additional information concerning the effect of mutual interference between body- and wing-induced velocity fields was obtained by testing the wing in combination with a body having a cylindrical mid-section.

It should be recognized that the present method of body contouring is primarily concerned with eliminating the interference at the root of a swept wing. The present method should not be confused with the methods of references 8 and 9, which are based on altering the axial distribution of cross-sectional area to minimize the wave drag at Mach numbers of 1 or greater.

NOTATION

A	aspect ratio
b	wing span
C_D	drag coefficient, $\frac{\text{drag}}{qS}$
C_L	lift coefficient, $\frac{\text{lift}}{qS}$
C_m	pitching-moment coefficient, $\frac{\text{pitching moment about } \bar{c}/4}{qS\bar{c}}$
c	local wing chord
\bar{c}	wing mean aerodynamic chord, $\frac{\int_0^{b/2} c^2 dy}{\int_0^{b/2} c dy}$
c_j	chord at wing-body junction (chord through the point of intersection of basic body and midchord line of the swept wing)
d_0	maximum body diameter
l	body length (distance from nose to theoretical point of closure)
M	free-stream Mach number
M_{cr}	wing critical Mach number based on simple-sweep concepts
M_{des}	design Mach number
P	pressure coefficient, $\frac{(\text{local static pressure}) - (\text{free-stream static pressure})}{q}$
q	free-stream dynamic pressure, $\frac{1}{2}\rho V_0^2$
r	body radius
r_0	maximum body radius
r_j	radius of basic body at intersection with midchord line of swept wing

S	wing area
$\frac{t}{c}$	wing thickness-to-chord ratio
u	streamwise perturbation velocity
V_0	free-stream velocity
x	distance behind body nose
y	lateral distance from model center line
Z	ordinate of wing surface, dimensionless with respect to the local wing chord
z	vertical distance above model center line
α	angle of attack
β	$\sqrt{1 - M^2}$
β_{des}	$\sqrt{1 - M_{des}^2}$
λ	wing taper ratio
Λ	angle of sweep, positive when swept back
Λ_e	effective angle of sweep, $\tan \Lambda_e = \frac{\tan \Lambda}{\beta_{des}}$
ξ	distance behind the leading edge of the wing-body junction, dimensionless with respect to the wing chord at the wing-body junction
ρ	free-stream mass density
Δr	radial modification associated with the vortex cylinder
Δr_y	modification to basic body radius in horizontal plane of symmetry
Δr_z	modification to basic body radius in vertical plane of symmetry

APPARATUS AND MODELS

Apparatus

The tests were conducted in the Ames 16-foot high-speed wind tunnel with the models mounted on a sting support as shown in figure 1. The normal and chord forces and the pitching moment were measured with electrical strain gages enclosed within the model. Multiple-tube mercury manometers, connected to pressure orifices in the model by flexible tubing, were photographed to provide records of the pressure distribution on the model surface.

Models

In this report, for reasons of brevity, those models designed without consideration of the wing-body interference problem are designated as "basic" and those designed with consideration of the interference problem are designated as "modified." The wing used in combination with the various bodies had an aspect ratio of 6, a taper ratio of 0.5, and NACA 64₂A015 sections normal to the 50-percent-chord line, which was swept back 35°. (See fig. 2.) For all the wing-body combinations tested, the center lines of the bodies were located in the chord plane of the wing, except for the model shown in figure 2(c) which was tested with the wing chord plane at the body center line and also with it 16.1 percent of the maximum body diameter above the body center line.

Configurations having basic bodies.— The bodies of revolution shown in figures 2(a), 2(b), 2(c), and 2(d) were shaped in accordance with the Sears-Haack formula

$$\frac{r}{r_0} = \left[1 - \left(1 - \frac{x}{l/2} \right)^2 \right]^{3/4}$$

except for the afterportion of the model shown in figure 2(b) where straight-line elements were used as shown.

The model shown in figure 2(e) had a body with a cylindrical midsection approximately twice the length of the wing root chord. The body radii forward and aft of the cylindrical midsection were computed using the Sears-Haack formula for which the corresponding values for $l/2$ were taken as the body length forward and aft of the cylindrical midsection, respectively, with r_0 equal to the cylinder radius.

All the bodies were truncated, as indicated in figure 2, in order to permit mounting on the sting. The fineness ratios of the bodies were

computed using the theoretical length of the body to closure and the maximum body diameter.

Configurations having modified bodies.- The bodies chosen for modification were those shown in figures 2(a), 2(c), and 2(d). These bodies were contoured in the vicinity of the wing-body junction so as to minimize the interference velocities at the design Mach number, 0.87, which was equal to the predicted critical Mach number of the swept wing (based on simple-sweep concepts).

A summary of the method for calculating the body modifications is given in the Appendix. The resultant bodies were not bodies of revolution in the vicinity of the wing-body junction but were elliptical in cross section. Details of the contouring are presented in figure 3. (See also the photographs in fig. 1.)

The basic bodies chosen for modification were also tested without the wing in order that the predicted body pressures, used in the contouring calculations, could be compared with measured body pressures.

TESTS AND PROCEDURE

The models were investigated through a Mach number range from 0.50 to 0.94, with a corresponding Reynolds number variation (based on the wing mean aerodynamic chord) from 2.6×10^6 to 3.4×10^6 (fig. 4). The test data have been corrected for the effects of blockage and tunnel-wall constraint by the methods of references 11 and 12.

The base drag, computed from the base areas of the bodies and the difference between measured base pressures and the free-stream static pressure, has been subtracted from the drag measurements. The drag data are believed to be slightly in error due to an interaction of the normal force and pitching moment on the chord-force measurements of the balance. This interaction was known to be small and inconsistent so no correction could be applied.

RESULTS AND DISCUSSION

Force Studies

The lift, drag, and pitching-moment data are shown in figure 5 for the nine configurations. Cross plots of these data, which summarize the drag, lift, and static longitudinal stability of the models, are presented in figures 6 to 9.

Drag.- It is apparent from the basic data shown in figure 5 that the drag for the configurations having modified bodies was much less than that for the basic configurations at Mach numbers above the critical (the predicted critical Mach number for the swept wing, based on simple-sweep concepts, is approximately 0.87). Modifying the bodies also resulted in reductions in drag at the higher lift coefficients for free-stream Mach numbers slightly less than 0.87. The zero-lift drag at subcritical Mach numbers was not greatly affected by the contouring.

The body modification increased the Mach number for drag divergence, defined as the Mach number for which

$$\left(\frac{dC_D}{dM} \right)_{C_L=0} = 0.1$$

by approximately 0.02. (See fig. 6.) More striking, however, was the reduction in drag above the divergence Mach number, the reduction in zero-lift drag at a Mach number of 0.94 being of the order of 40 percent.

The drag for the wing in the rearward position was only slightly less than that for the wing in the forward position (fig. 6(a)). The configuration having a body with cylindrical midsection, when compared with the one using the basic body of the same size, had less drag at Mach numbers above the critical but slightly greater drag at subcritical speeds (fig. 6(b)). Raising the wing did not affect the zero-lift drag (fig. 6(c)). The same effects are shown for a lift coefficient of 0.3 in figure 7.

Lift.- The variation of lift-curve slope (evaluated at zero lift) with Mach number is shown in figure 8. Although minor differences in lift-curve slope for the various basic and modified models are evident at low Mach numbers, the most significant effects occurred at Mach numbers near and above the critical. Modifying the body shape resulted in less variation of lift-curve slope with Mach number and an increase in the lift-curve slope at supercritical Mach numbers.

A comparison of the data for the models with the wing forward and with the wing aft (fig. 8(a)) indicates that the lift-curve slope for the model with the wing aft rose to a somewhat lower maximum value near the critical Mach number but then decreased in a somewhat similar manner with increasing supercritical Mach number. The model having a body with a cylindrical midsection had a slightly lower lift-curve slope at low speeds than the basic body of the same size (fig. 2(d)). The maximum slope was reached at a Mach number slightly greater than that for the basic body, but the rate of change of lift-curve slope with increasing supercritical Mach number was greater (fig. 8(b)). Raising the wing to a position above the center line of the body did not affect the lift-curve slope (fig. 8(c)).

Moment.- The variation of the static longitudinal stability parameter, $\left(\frac{\partial C_m}{\partial C_L} \right)_{C_L=0}$, with Mach number is presented in figure 9.

Modifying the body shape resulted in smaller changes in the stability parameter with changes in Mach number.

The longitudinal position of the wing with respect to the body had a large effect on the stability parameter (fig. 9(a)). The change in stability occurring with increasing Mach number was most pronounced with the wing in a rearward position. The effect of replacing the midsection of the body by a cylinder was relatively unimportant (fig. 9(b)). Raising the wing resulted in small changes in the stability parameter (fig. 9(c)).

Pressure Studies

The effects of the body modification on the pressure distribution over the inner half of the wing at zero angle of attack are illustrated in figure 10 for three high subsonic Mach numbers. With the basic bodies the wing pressures near the root were less negative than those along the outer panel of the wing, but, as predicted by theory, an unfavorable distortion of the pressure distribution occurred near the root, the location of the point of minimum pressure being shifted rearward.

The bodies had been modified in an attempt to obtain the same pressure distribution near the root chord as over the outer portion of the wing. Although this was far from being accomplished, a more favorable distribution of pressure over the root was obtained. Specifically, the point of most negative pressure was moved from a position behind the root midchord to a position forward of the midchord. The influence of the body modifications extended to a considerable distance from the root, and the absence of severe pressure gradients near the trailing edge of the inner portion of the wing is particularly noteworthy.

CONCLUDING REMARKS

These tests show that a considerable improvement in the aerodynamic characteristics of wing-body combinations, employing a swept wing of large thickness-to-chord ratio and large aspect ratio, can be obtained at high-subsonic Mach numbers by contouring the body in the vicinity of the wing-body junction according to the ring-vortex design method suggested by Küchemann. This type of body modification did not significantly

affect the aerodynamic characteristics at Mach numbers below the critical of the swept wing. At Mach numbers above the critical, improved aerodynamic characteristics were evidenced by large reductions of drag, an increase in lift-curve slope, and a reduced change of pitching-moment-curve slope with increasing Mach number. Vertical and longitudinal changes of the position of the wing on the body had little effect on the aerodynamic characteristics of the unmodified wing-body combinations.

Ames Aeronautical Laboratory
National Advisory Committee for Aeronautics
Moffett Field, Calif., Jan. 22, 1954

APPENDIX

METHOD OF BODY MODIFICATION

The design objective is to alter the body shape so that the velocity distribution at zero lift, for a given subsonic Mach number, will be the same at the wing-body junction as that on an infinite yawed wing at the same Mach number. Computations of the required body contours are based on a method proposed by Küchemann (refs. 6 and 7) in which linearized theory is used throughout.

Perturbation Velocities at the Wing-Body Junction

The streamwise perturbation velocity u_j in the plane of the wing and at the wing-body junction is regarded as being composed of the following additive components:

$$\frac{u_j}{V_0} = \frac{u_b}{V_0} + \frac{u_w}{V_0} + \frac{u_c}{V_0} + \frac{u_m}{V_0} \quad (A1)$$

where

u_b perturbation velocity induced by a body alone

u_w perturbation velocity of an infinite yawed wing

u_c distortion velocity at the root of a swept wing¹

u_m perturbation velocity induced by modifications of the basic body shape

In order that the velocity at the wing-body junction be the same as for an infinite yawed wing, it is necessary that the body modification result in a perturbation velocity of sufficient strength to cancel the sum of the body perturbation velocity u_b and the wing-root distortion velocity u_c ; that is, the condition

$$\frac{u_m}{V_0} = - \left(\frac{u_c}{V_0} + \frac{u_b}{V_0} \right) \quad (A2)$$

is to be satisfied along the wing-body junction (reference chord).

¹In this procedure the body is considered to be a reflection plane.

Design Mach Number

In general, the compressibility corrections will be different for the two velocity ratios u_c/V_0 and u_b/V_0 to be canceled by means of the body modification. Because the variation with Mach number is different for these two velocity ratios, it is necessary to select a design Mach number for use in computing the body modification. The most beneficial results of the body contouring are expected at supercritical speeds; therefore, it seems rational to use the critical Mach number of the yawed wing as the design Mach number, since this is the highest subsonic Mach number for which linearized theory can be expected to give reasonable results. The NACA 64₂015 airfoil used has a theoretical critical Mach number of 0.87 when yawed 35°.

Body-Induced Velocities

The body-induced velocities may be computed by means of any of the methods proposed for bodies of revolution in axially symmetric flow. The slender-body approximation of Laitone (ref. 13) is used here.² The formula is

$$\frac{u_b}{V_0} = -\frac{1}{2\pi} \left\{ \left(\frac{1 - \frac{2x}{l}}{1 - \frac{x}{l}} \right) \frac{S'(x)}{2x} - \left[1 + \ln \frac{\beta r}{l} - \ln 2 \sqrt{\frac{x}{l} \left(1 - \frac{x}{l} \right)} \right] S''(x) \dots \right\} \quad (A3)$$

where $S(x)$ is the cross-sectional area of the body and $S^{(n)}(x)$ is the n th derivative of this area with respect to x . The body equation for use in equation (A3) is, for the bodies of this report, the Sears-Haack formula

$$\frac{r}{r_0} = \left[1 - \left(1 - \frac{2x}{l} \right)^2 \right]^{3/4} \quad (A4)$$

It should be noted that equation (A3) includes the effect of compressibility. The first two terms are sufficient to give a reasonably

²The use of Laitone's method, which depends on expanding the expression for the cross-sectional area of the body in a power series, is permissible here because the bodies used are described by an analytically continuous function.

good prediction of the body-induced velocities near the center section of slender bodies. A comparison of calculated and measured body pressures is presented in figure 11.

Distortion Velocity at the Root of a Swept Wing

The velocity near the root of a swept wing is known to be distorted from that of an infinite yawed wing. Küchemann has determined the magnitude of the distorting velocity at the root of an untapered wing of infinite aspect ratio in incompressible flow to be

$$-\frac{u_c(\xi)}{V_0} = \frac{\cos \Lambda \frac{dZ(\xi)}{d\xi}}{\pi} \ln \frac{1 + \sin \Lambda}{1 - \sin \Lambda} \quad (A5)$$

where $Z(\xi)$ is the ordinate of the airfoil surface, made dimensionless with respect to the wing chord, and Λ is the angle of sweep (positive when swept back).

For compressible flow, the three-dimensional form of the Prandtl-Glauert transformation (ref. 14) is applied to equation (A5). At a given design Mach number, M_{des} , equation (A5) becomes

$$-\left(\frac{u_c(\xi)}{V_0}\right)_{des} = \frac{\cos \Lambda_e \frac{dZ}{d\xi}}{\pi \beta_{des}} \ln \frac{1 + \sin \Lambda_e}{1 - \sin \Lambda_e} \quad (A6)$$

where

$$\beta_{des} = \sqrt{1 - M_{des}^2}$$

and the effective angle of sweep is related to the actual sweep angle by

$$\tan \Lambda_e = \frac{\tan \Lambda}{\beta_{des}}$$

The distortion velocity at the root of the 35° swept wing used in the present investigation is shown in figure 12. The effects of taper and aspect ratio for this wing are believed to be small and were neglected. The slope of the airfoil surface was determined graphically.

Body Modification

The body is replaced by a vortex cylinder, that is, a cylinder upon which ring vortices are distributed so as to induce an axial-velocity ratio u_m/V_0 of sufficient strength to cancel the velocity ratios u_b/V_0 and u_c/V_0 . The vortex cylinder is assumed to be of constant radius, r_j , equal to the body radius at the midpoint of the reference chord (at the wing-body junction) and of length, c_j , equal to the length of the reference chord. (See fig. 3.)

Six standard distributions of vortex rings, suitable for the design of wing-body intersection lines, and the corresponding induced velocities, are given in reference 7. The distribution functions are:

Even functions

$$\frac{\gamma_2}{\gamma_{02}} = \sqrt{1 - (2\xi - 1)^2}$$

$$\frac{\gamma_6}{\gamma_{06}} = \sqrt[4]{1 - (2\xi - 1)^2}$$

$$\frac{\gamma_8}{\gamma_{08}} = 1 - (2\xi - 1)^2$$

Odd functions

$$\frac{\gamma_3}{\gamma_{03}} = - (2\xi - 1) \sqrt{1 - (2\xi - 1)^2}$$

$$\frac{\gamma_7}{\gamma_{07}} = - (2\xi - 1) \sqrt[4]{1 - (2\xi - 1)^2}$$

$$\frac{\gamma_9}{\gamma_{09}} = - (2\xi - 1) \left[1 - (2\xi - 1)^2 \right]$$

Here, a coordinate system is used in which ξ is made dimensionless with respect to the reference chord, positive when directed downstream and with origin at the leading edge of the reference chord. The functions γ_v/γ_{0v} are plotted in figure 13.

The distribution of ring-vortex strength along the cylinder is determined by equating the induced axial velocity ratio to the value of

$$-\left(\frac{u_b + u_c}{V_o}\right) \text{ at a number of control points along the reference chord.}$$

The corresponding radial component of induced velocity is then used to determine the body-shape modification Δr .

The axial velocity induced by the vortex cylinder can be represented by

$$\frac{u_m}{V_o} = \sum_v C_v \left(\frac{u_v^*}{V_o} - \pi \frac{\gamma_v}{\gamma_{ov}} \right) \quad (A7)$$

and the radial increment Δr by

$$\frac{\Delta r}{c_j/2} = \sum_v C_v \left(\frac{\Delta r_v^*}{c_j/2} \right) \quad (A8)$$

where γ_v/γ_{ov} , u_v^*/V_o , and $\Delta r_v^*/(c_j/2)$ are functions tabulated in tables III, IV, and VI, respectively, of reference 7 for various values of the vortex-cylinder length-to-diameter ratio. (Values of x in the tables of reference 7 correspond to values of $2\xi - 1$ in the notation used here.)

Since there are six vortex distribution functions to be used, the velocity ratio u_m/V_o must be evaluated at six chordwise control points. For the work of this report, control points at $\xi = 0.1, 0.3, 0.5, 0.6, 0.7$, and 0.9 were chosen. The tables in reference 7, which are for

$M = 0$, may be used directly if the velocity ratio $\left(\frac{u_b + u_c}{V_o}\right)$ is reduced

by β_{des} and if a vortex cylinder of reduced radius $\beta_{des} r_j$ is used. (See ref. 14.) Equation (A7) may then, with the help of tables III and IV in reference 7, be applied at each control point and the resulting system of six equations can be solved simultaneously for the six unknown coefficients C_v . When the coefficients C_v are known, the modification Δr can then be calculated by using equation (A8), for which tabulated values of $\Delta r_v/(c_j/2)$ are to be found in table VI of reference 7.

As an illustration, the radial modifications for the body having a fineness ratio of 12 (wing in the forward position) are shown in figure 14(a). It is readily seen that the radial modification (calculated by summing the odd and even functions) rapidly approaches zero upstream and downstream of the reference chord. For application in the present method of body contouring, the value at $\xi = -0.2$ was subtracted in order to start the modification at that point, and an arbitrary fairing was used to terminate the modification at $\xi = 1.2$. (See fig. 14(b).)

Additional Modification

In the preceding development, the vortex intensity was constant around the periphery of each cylindrical cross section, so the calculated changes in body radius resulted in annual bumps, invariant with position around the circle. The major portion of the "interference velocity" u_m , however, is attributable to the wing and attenuates rapidly in the vertical direction. An approximation for the attenuation at the top of the body was obtained by considering the variation with vertical distance of the maximum perturbation velocity induced by a two-dimensional, unswept, biconvex airfoil. According to linearized theory, this variation is

$$\left(\frac{u}{V_0}\right)_{\max} = \frac{4t/c}{\beta\pi} \left(1 - \frac{2\beta z}{c} \tan^{-1} \frac{c}{2\beta z}\right) \quad (A9)$$

With this expression as a guide, the radial modification at the top of the body was reduced by the amount

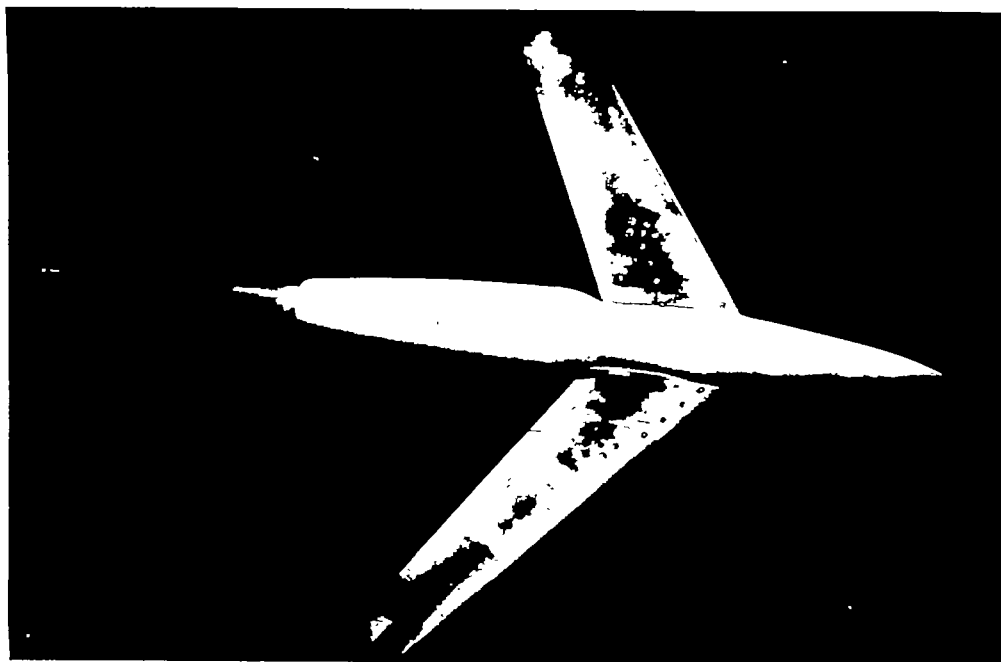
$$\frac{\Delta r_z}{\Delta r} = 1 - \frac{2\beta_{des} r_j}{c_j} \tan^{-1} \frac{c_j}{2\beta_{des} r_j} \quad (A10)$$

and the contoured body shape was made elliptical in cross section with the full radial increment at the side, so that $\Delta r_y = \Delta r$. Details of the contoured bodies are presented in figure 3.

REFERENCES

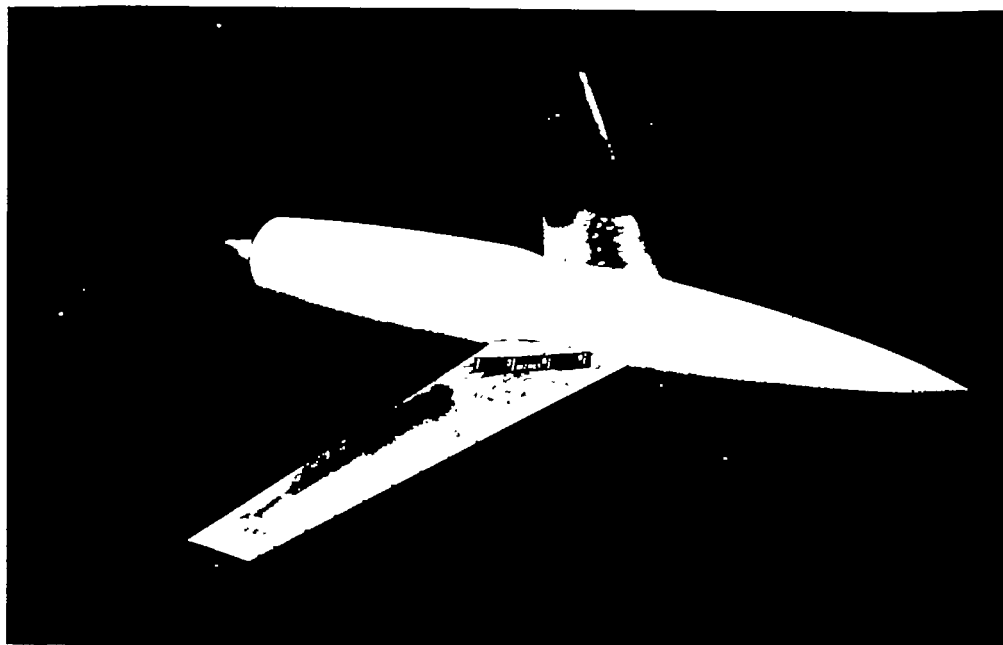
1. Jones, R. T.: Subsonic Flow over Thin Oblique Airfoils at Zero Lift. NACA Rep. 902, 1948. (Supersedes NACA TN 1340)
2. Neumark, S.: Velocity Distribution on Straight and Sweptback Wings of Small Thickness and Infinite Aspect Ratio at Zero Incidence. R.A.E. Rep. No. Aero. 2200, British, 1947.
3. Watkins, Charles E.: The Streamline Pattern in the Vicinity of an Oblique Airfoil. NACA TN 1231, 1947.
4. Boddy, Lee E.: Investigation at High Subsonic Speeds of Methods of Alleviating the Adverse Interference at the Root of a Swept-Back Wing. NACA RM A50E26, 1950.
5. Pepper, William B., Jr.: The Effect on Zero-Lift Drag of an Indented Fuselage or a Thickened Wing-Root Modification to a 45° Swept-Back Wing-Body Configuration as Determined by Flight Test at Transonic Speeds. NACA RM L51F15, 1951.
6. Küchemann, D.: Design of Wing Junction, Fuselage and Nacelles to Obtain the Full Benefit of Sweptback Wings at High Mach Number. R.A.E. Rep. No. Aero. 2219, British, 1947.
7. Weber, J.: Design of Wing Junction, Fuselage and Nacelles to Obtain the Full Benefit of Sweptback Wings at High Mach Number. Addendum: Additional Tables of Coefficients. R.A.E. Rep. No. Aero. 2219(a), British, 1949.
8. Küchemann, D., and Weber, J.: The Calculation of Thin Ring Profiles. MAP Völkenrode MAP-VG 62.
9. Whitcomb, Richard T.: A Study of the Zero-Lift Drag-Rise Characteristics of Wing-Body Combinations Near the Speed of Sound. NACA RM L52H08, 1952.
10. Jones, Robert T.: Theory of Wing-Body Drag at Supersonic Speeds. NACA RM A53H18a, 1953.

12. Silverstein, Abe, and White, James A.: Wind-Tunnel Interference With Particular Reference to Off-Center Positions of the Wing and to the Downwash at the Tail. NACA Rep. 547, 1935.
13. Laitone, E. V.: The Linearized Subsonic and Supersonic Flow About Inclined Slender Bodies of Revolution. Jour. Aero. Sci., vol. 14, no. 11, Nov. 1947, pp. 631-642.
14. Göthert, B.: Plane and Three-Dimensional Flow at High Subsonic Speeds. NACA TM 1105, 1946. From: Lilienthal-Gesellschaft für Luftfahrtforschung, Berlin, Bericht 127, Sept. 1940, pp. 97-101.



A-16454

(a) General view of swept wing mounted on a modified small body having a fineness ratio of 9.



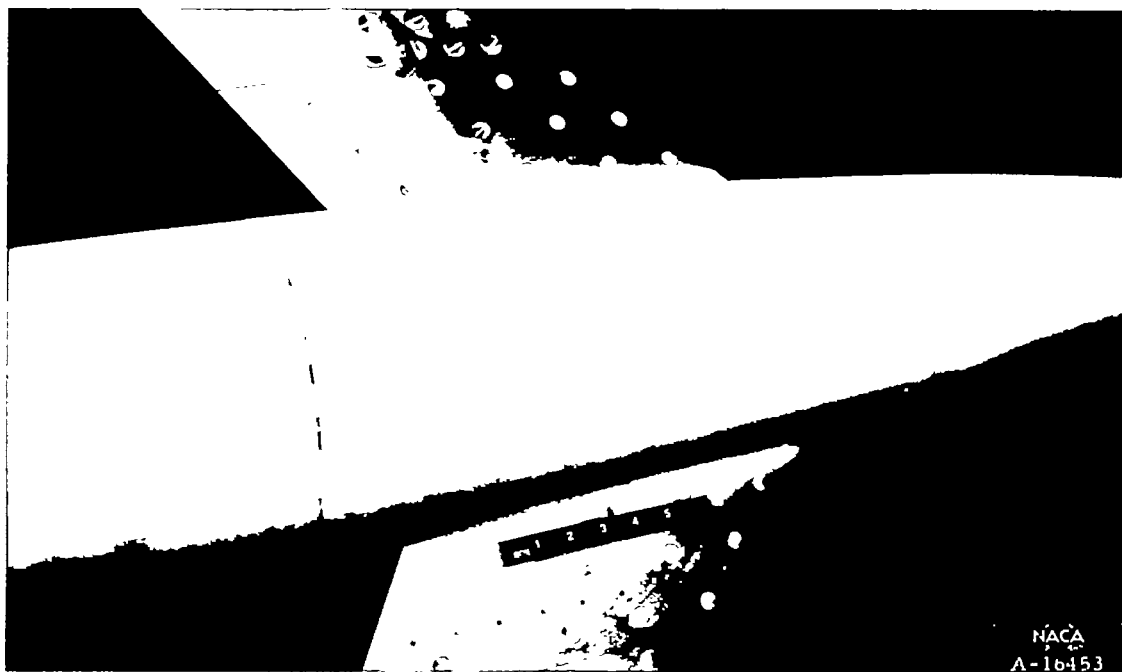
A-16451

(b) General view of swept wing mounted on a modified large body having a fineness ratio of 9.

Figure 1.- Photographs of the models.

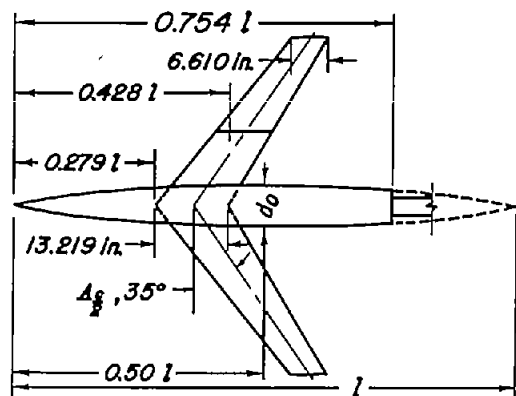


(c) Close-up of intersection of swept wing with modified large body having a fineness ratio of 9.

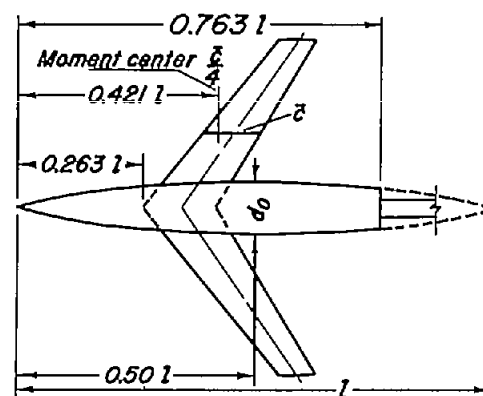


(d) Close-up of intersection of swept wing with basic large body having a fineness ratio of 9.

Figure 1.- Concluded.



(a) Body having a fineness ratio of 12 (wing forward).



(c) Large body having a fineness ratio of 9.

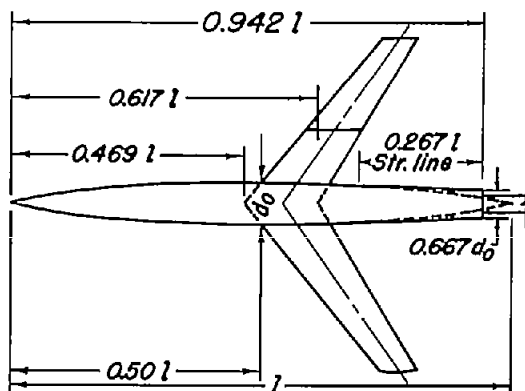
Body dimensions

Figure	l , in.	d_0 , in.
a	90.00	7.50
b	90.00	7.50
c	85.50	9.50
d	67.50	7.50
e	68.33	7.59

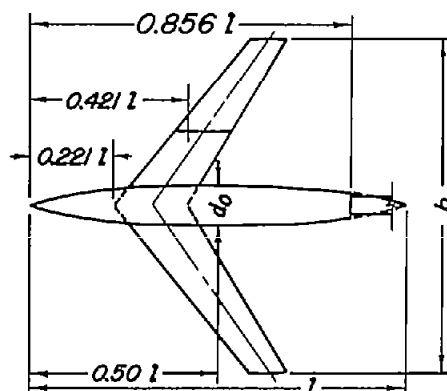
Wing geometry

S	4.131 sq ft
A	6.0
λ	0.5
b	60 in.
\bar{c}	10.28 in.

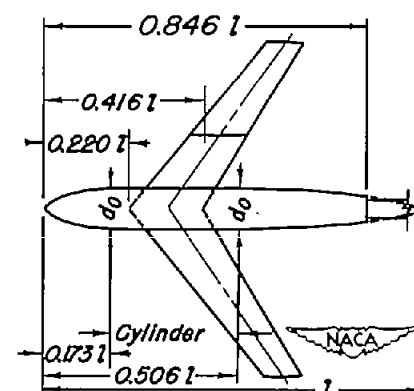
Airfoil section 64_e AO151 $\frac{8}{2}$



(b) Body having a fineness ratio of 12 (wing aft).

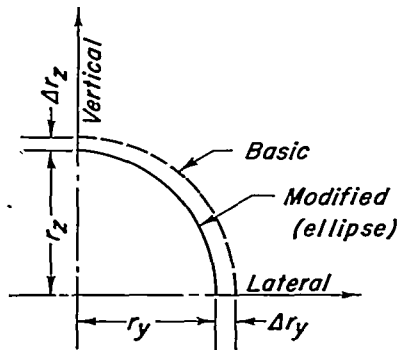
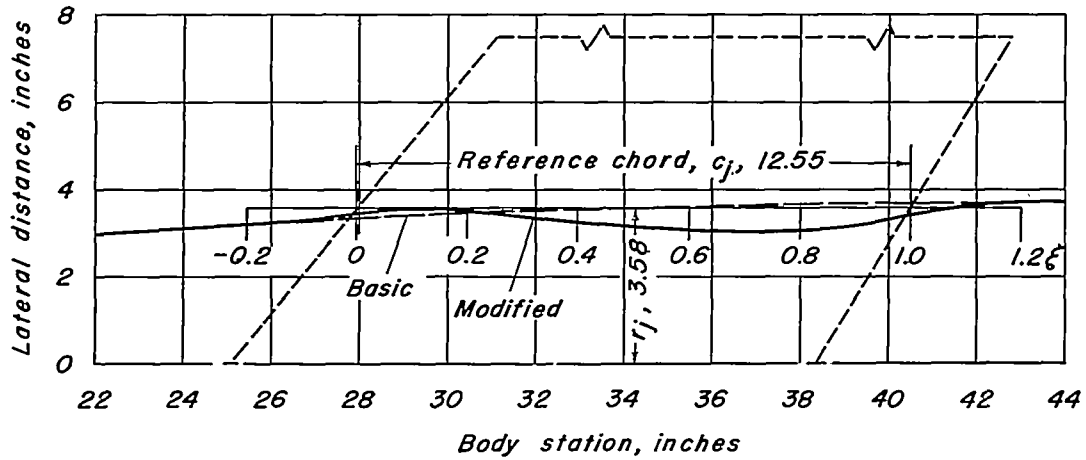


(d) Small body having a fineness ratio of 9.



(e) Cylindrical body having a fineness ratio of 9.

Figure 2.—Geometry of the basic models.



$$\frac{\Delta r_z}{\Delta r_y} = 0.63$$

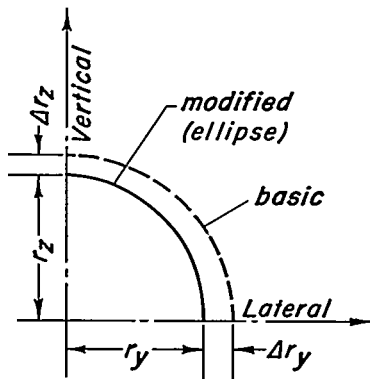
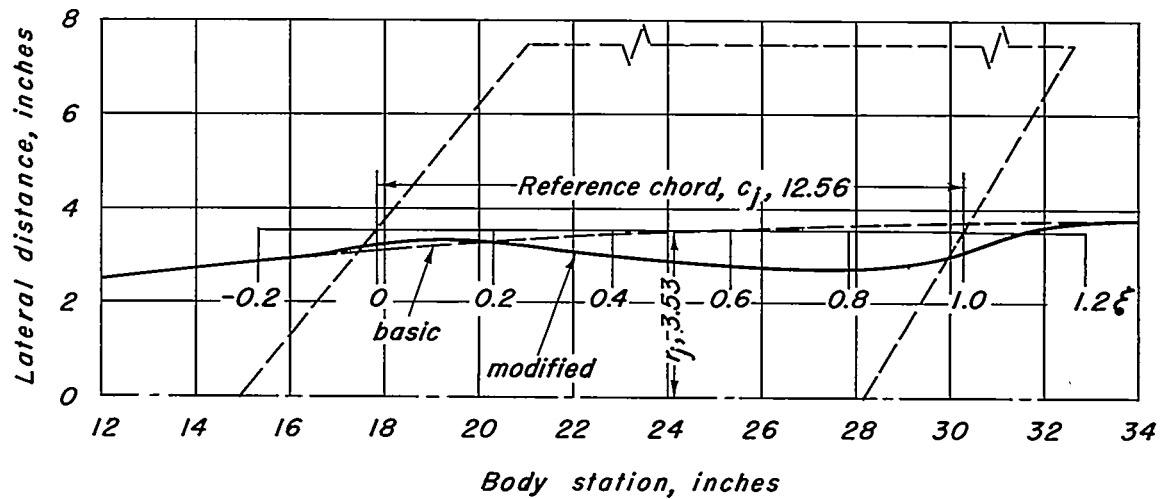
$$M_{des} = 0.87 = M_{cr}$$

Body station, inches	ξ	Basic body radius, inches	Modified body	
			r_y , inches	r_z , inches
25.43	-0.2	3.20	3.20	3.20
26.69	-.1	3.28	3.26	3.26
27.94	0	3.34	3.44	3.41
29.20	.1	3.40	3.57	3.50
30.45	.2	3.47	3.50	3.48
31.71	.3	3.51	3.37	3.42
32.96	.4	3.56	3.24	3.35
34.22	.5	3.58	3.13	3.30
35.48	.6	3.61	3.07	3.27
36.73	.7	3.65	3.03	3.26
37.99	.8	3.67	3.03	3.27
39.24	.9	3.70	3.18	3.38
40.49	1.0	3.72	3.42	3.53
41.75	1.1	3.73	3.63	3.67
43.00	1.2	3.75	3.75	3.75



(a) Body having a fineness ratio of 12. (See fig. 2(a).)

Figure 3.-Contouring details.



$$\frac{\Delta r_z}{\Delta r_y} = 0.65$$

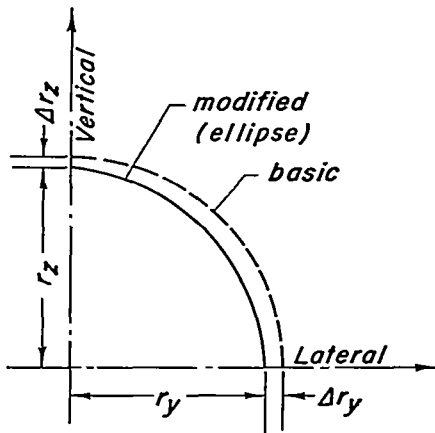
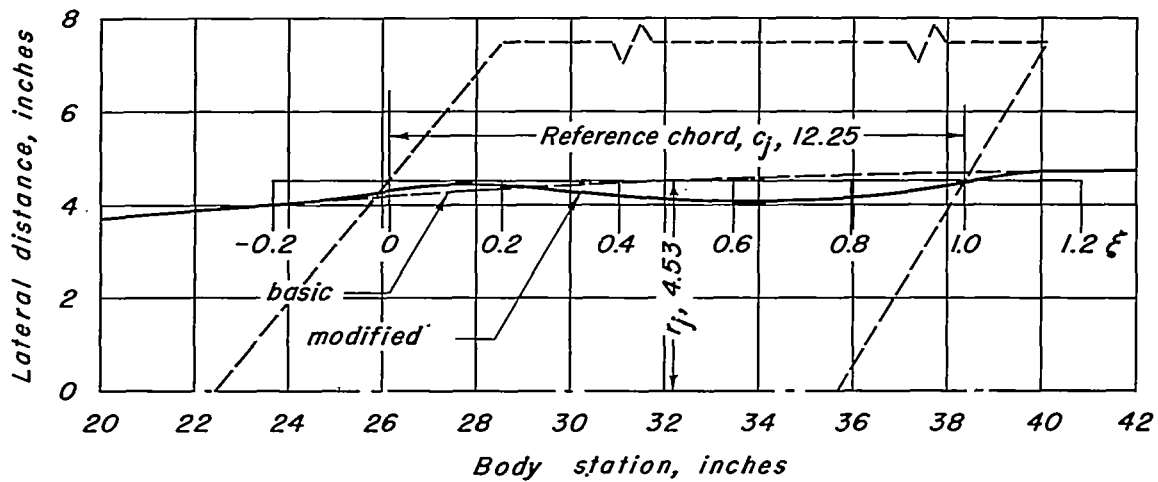
$$M_{des} = 0.87 = M_{cr}$$

Body station, inches	ξ	Basic body radius, inches	Modified body	
			r_y , inches	r_z , inches
15.31	-0.2	2.87	2.87	2.87
16.57	-.1	3.00	2.95	2.97
17.82	0	3.11	3.22	3.18
19.08	.1	3.21	3.34	3.30
20.33	.2	3.30	3.27	3.28
21.59	.3	3.39	3.13	3.22
22.84	.4	3.46	3.01	3.16
24.10	.5	3.53	2.89	3.10
25.35	.6	3.58	2.84	3.09
26.61	.7	3.62	2.74	3.05
27.86	.8	3.67	2.74	3.07
29.12	.9	3.70	2.78	3.10
30.38	1.0	3.72	3.13	3.34
31.63	1.1	3.74	3.56	3.62
32.89	1.2	3.75	3.73	3.75



(b) Small body having a fineness ratio of 9. (See fig. 2(d).)

Figure 3.-Continued.



$$\frac{\Delta r_z}{\Delta r_y} = 0.54$$

$$M_{des} = 0.87 = M_{cr}$$

Body station, inches	ξ	Basic body radius, inches	Modified body	
			r_y , inches	r_z , inches
23.68	-0.2	4.00	4.00	4.00
24.91	-.1	4.12	4.11	4.11
26.13	0	4.20	4.28	4.24
27.35	.1	4.28	4.43	4.36
28.57	.2	4.36	4.39	4.37
29.80	.3	4.43	4.33	4.37
31.02	.4	4.50	4.22	4.34
32.25	.5	4.53	4.14	4.32
33.47	.6	4.57	4.11	4.33
34.70	.7	4.62	4.12	4.35
35.93	.8	4.66	4.20	4.41
37.15	.9	4.68	4.27	4.46
38.38	1.0	4.71	4.57	4.64
39.60	1.1	4.72	4.72	4.73
40.83	1.2	4.74	4.74	4.74



(c) Large body having a fineness ratio of 9. (See fig. 2(c).)

Figure 3.—Concluded

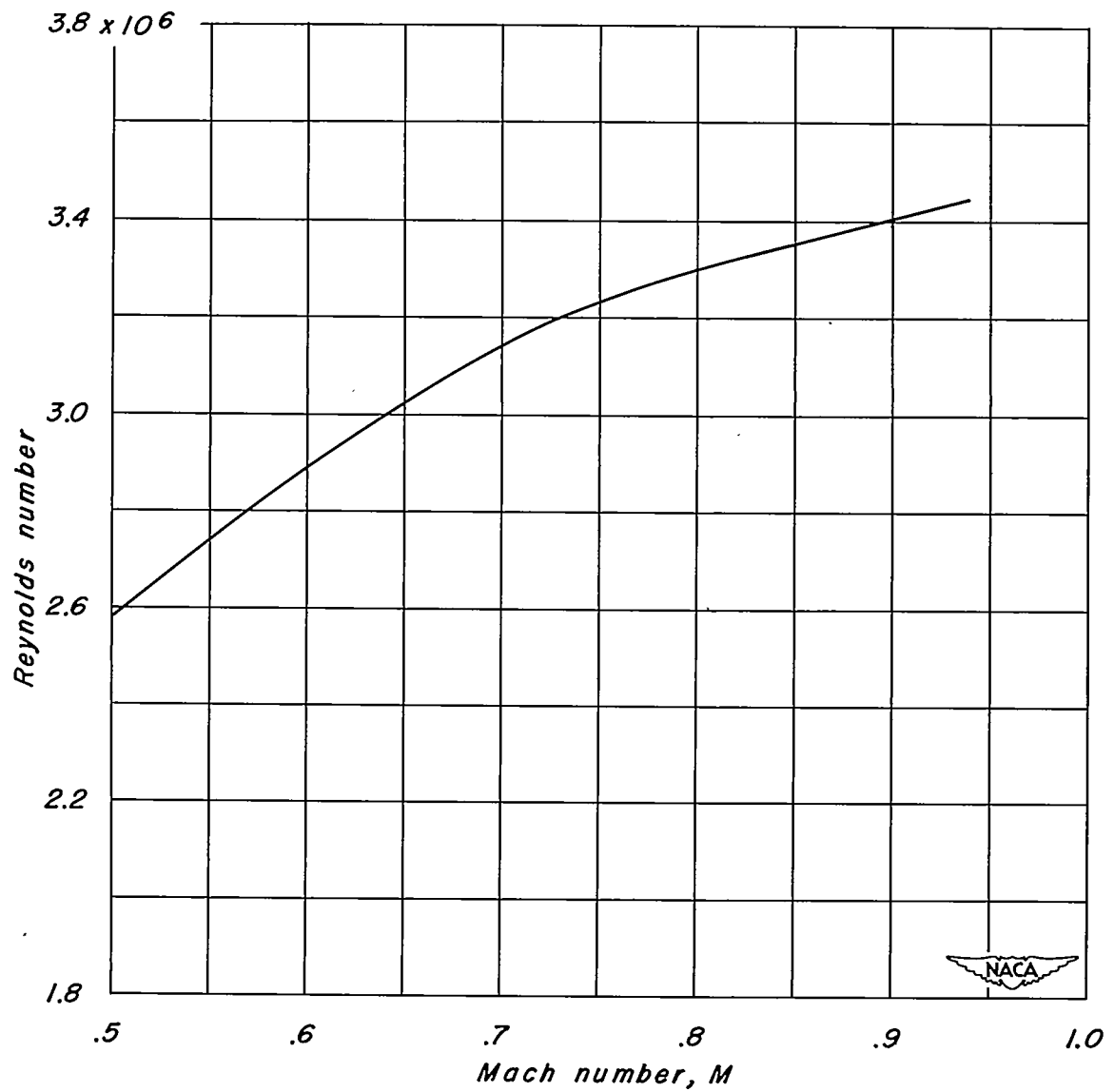
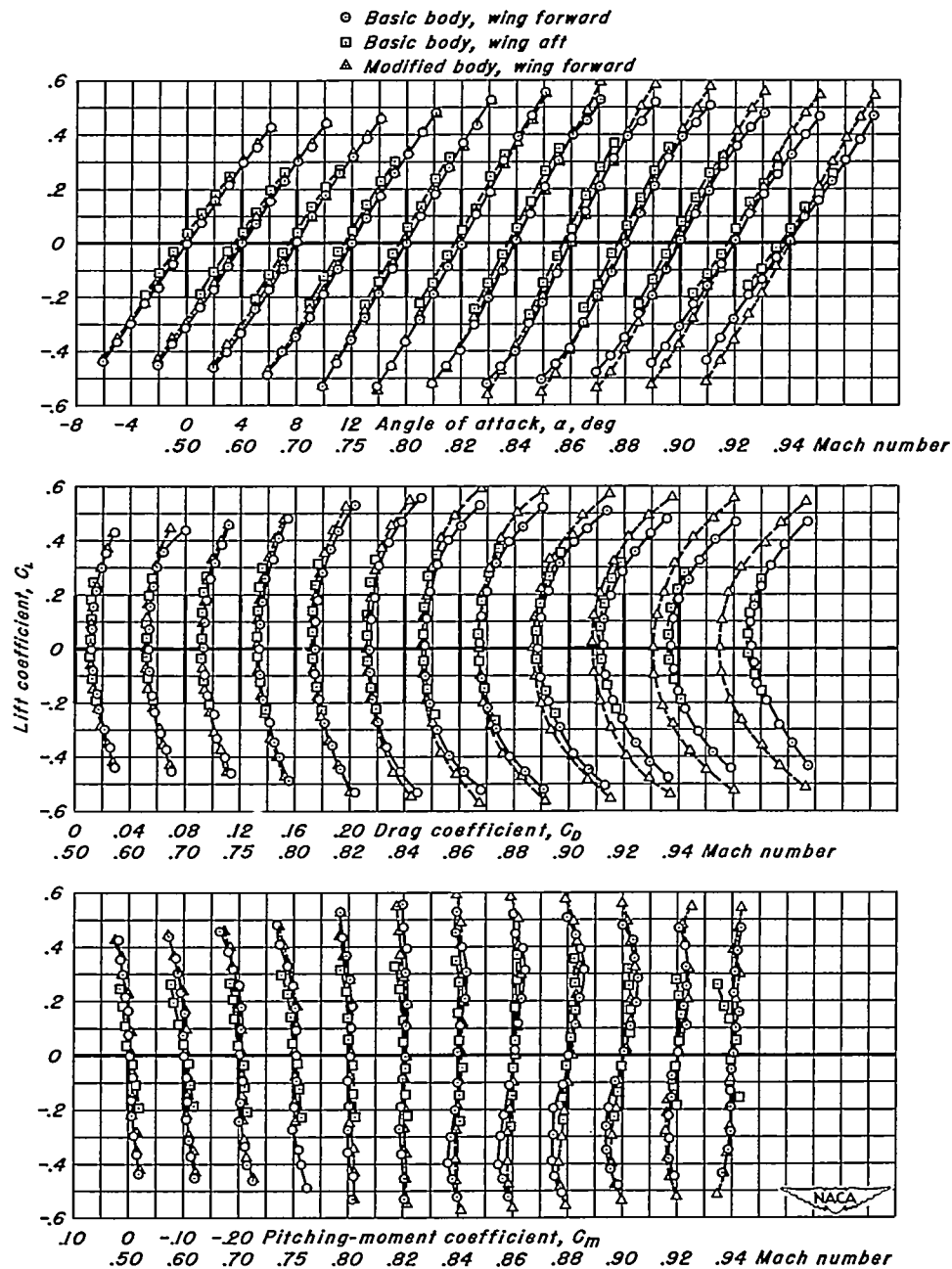
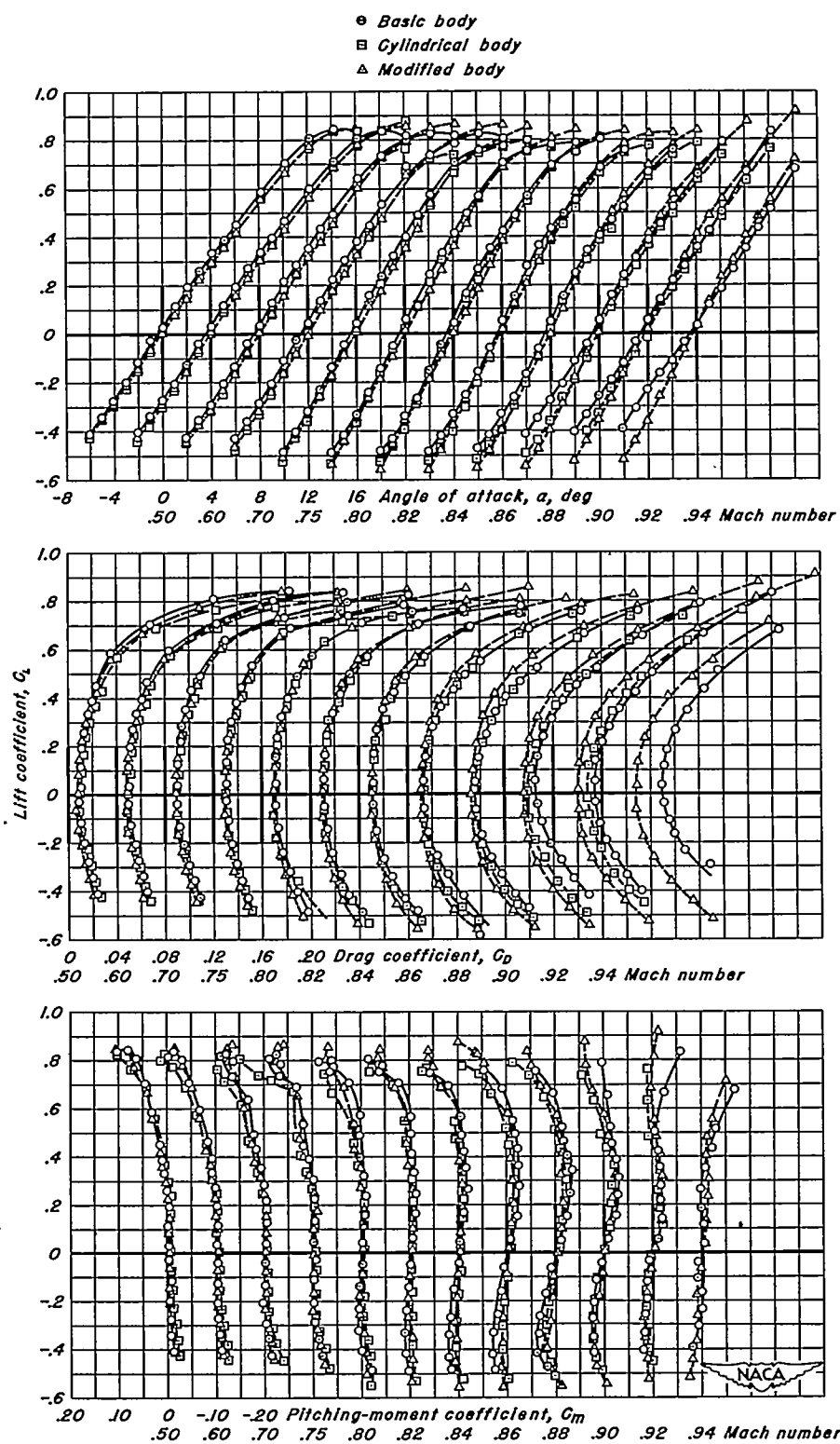


Figure 4.- Variation of Reynolds number with Mach number.



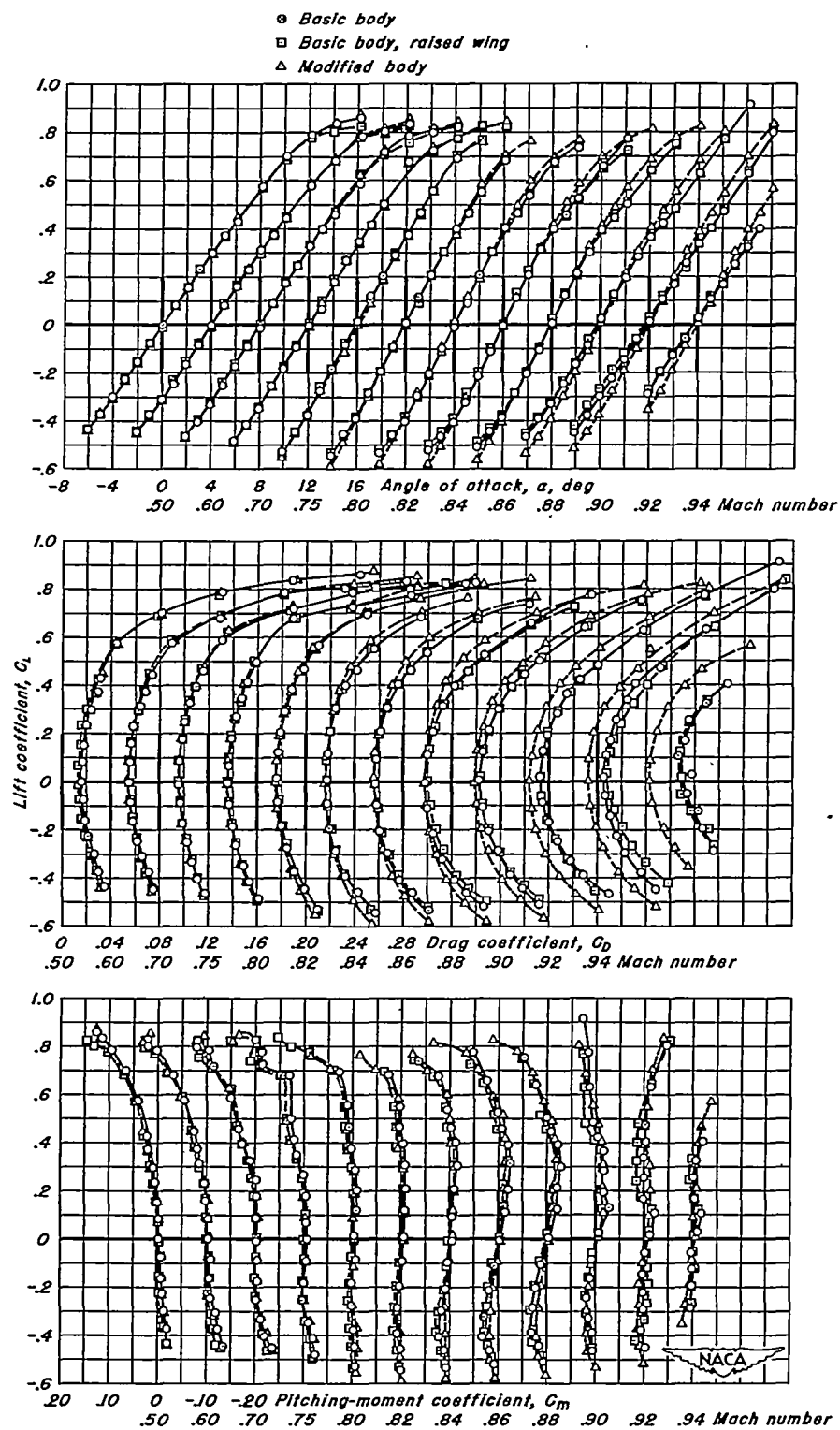
(a) Body with a fineness ratio of 12.

Figure 5. - Lift, drag, and pitching-moment characteristics for the sweptback wing in combination with various bodies.



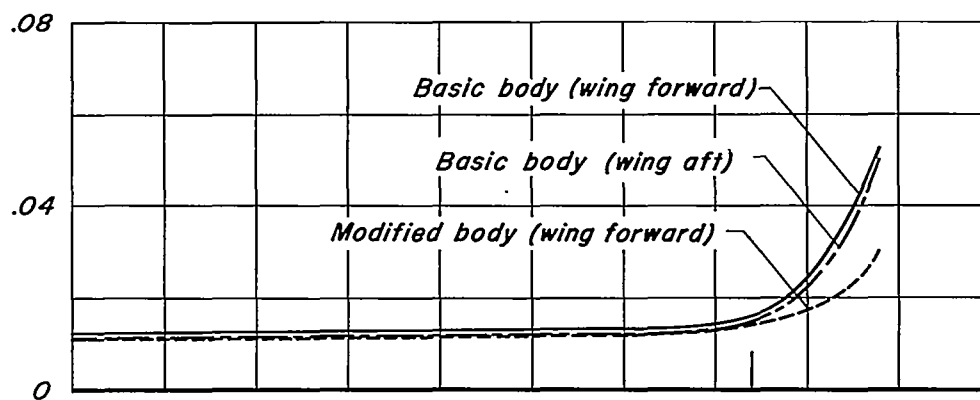
(b) Small body with a fineness ratio of 9.

Figure 5.—Continued.

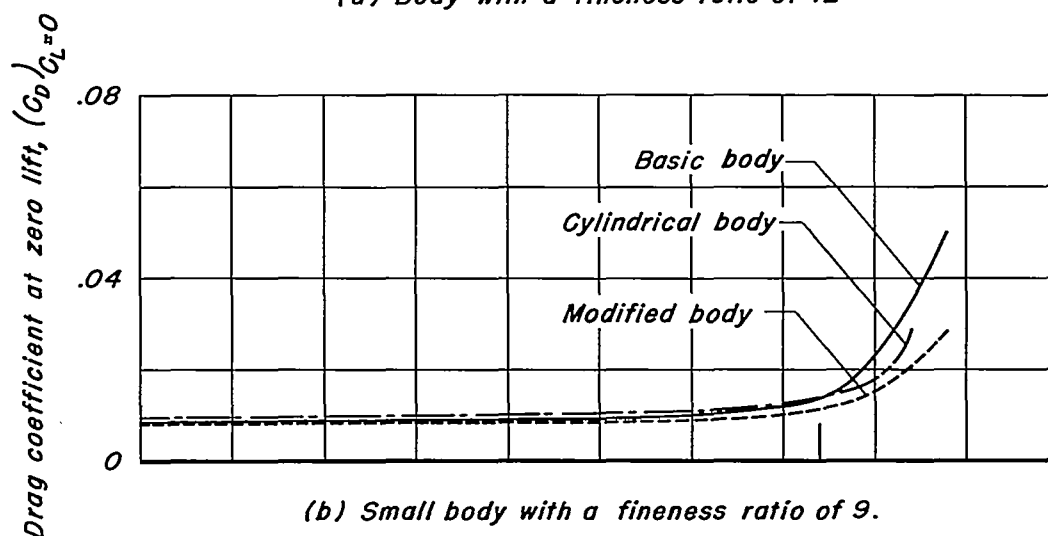


(c) Large body with a fineness ratio of 9.

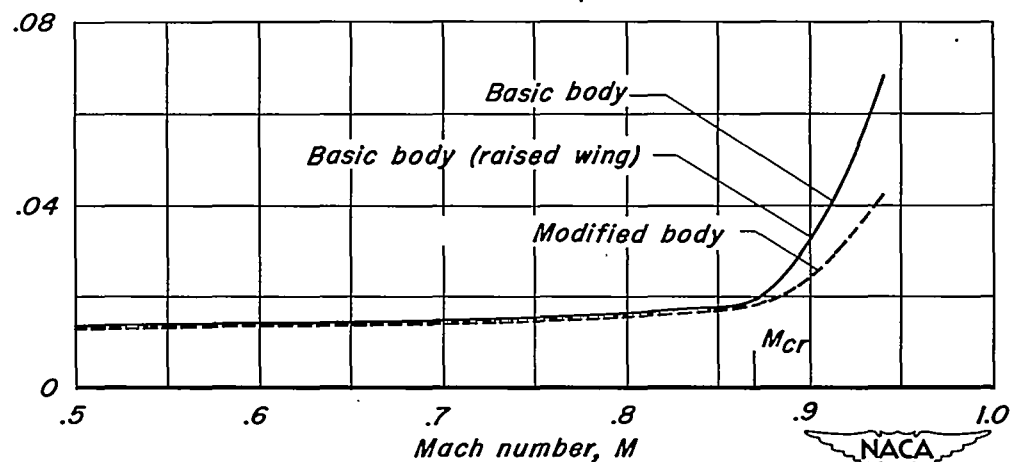
Figure 5.-Concluded.



(a) Body with a fineness ratio of 12



(b) Small body with a fineness ratio of 9.



(c) Large body with a fineness ratio of 9.

Figure 6.-Variation of drag coefficient at zero lift with Mach number for the swept wing in combination with various bodies.

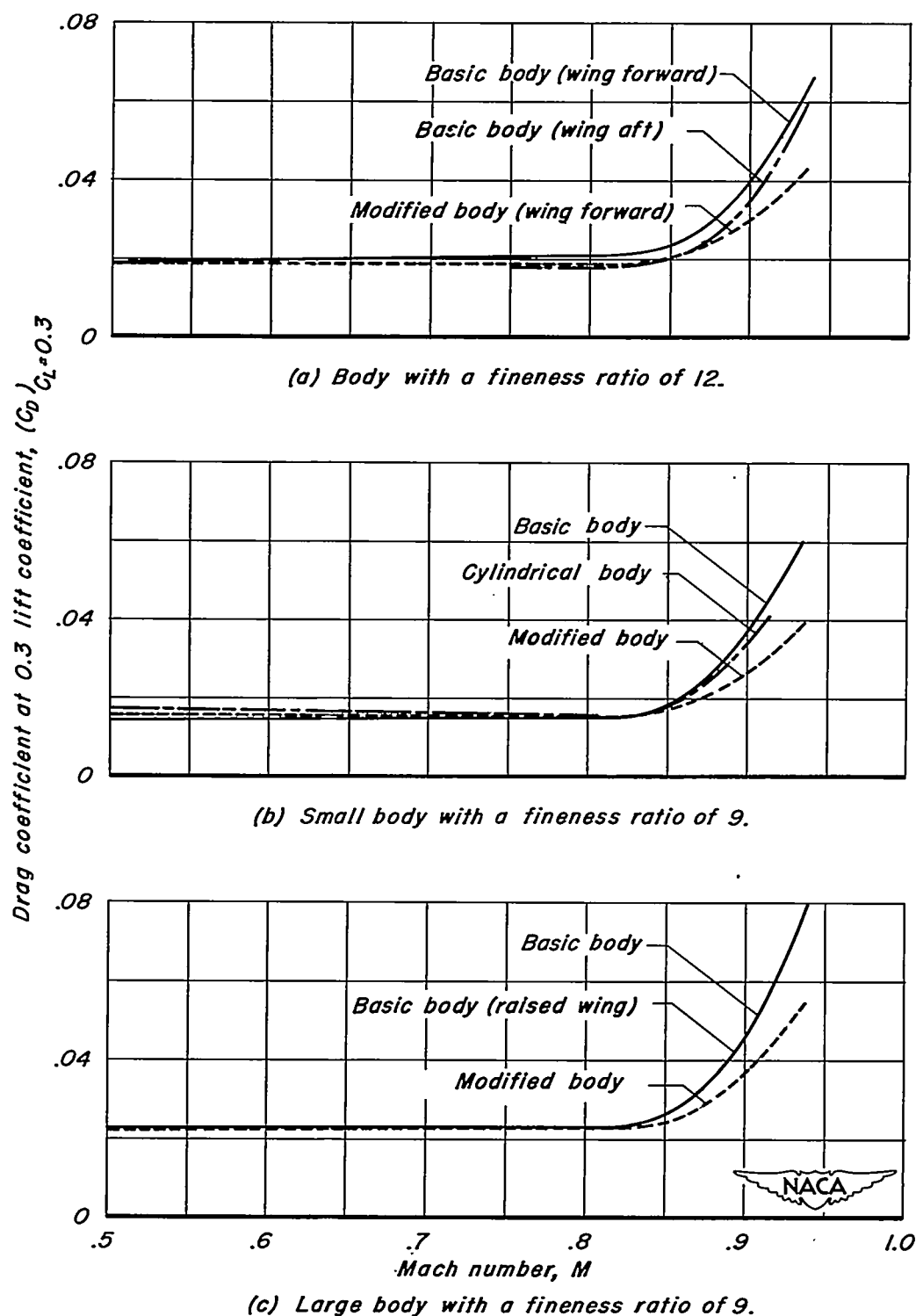
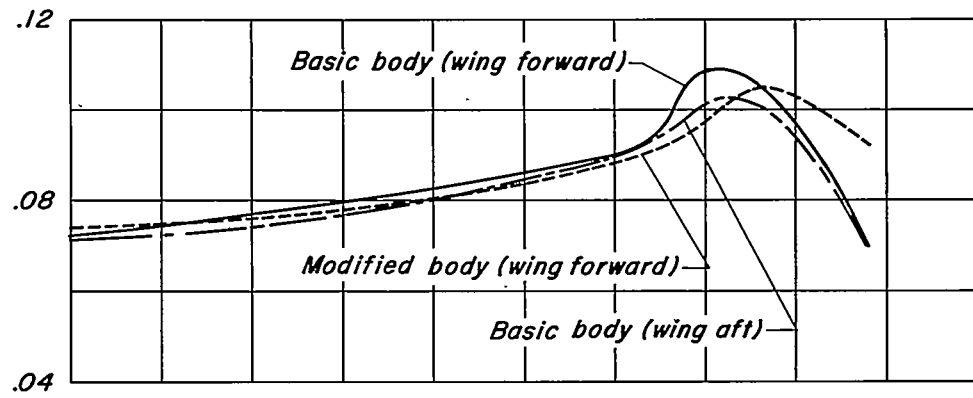
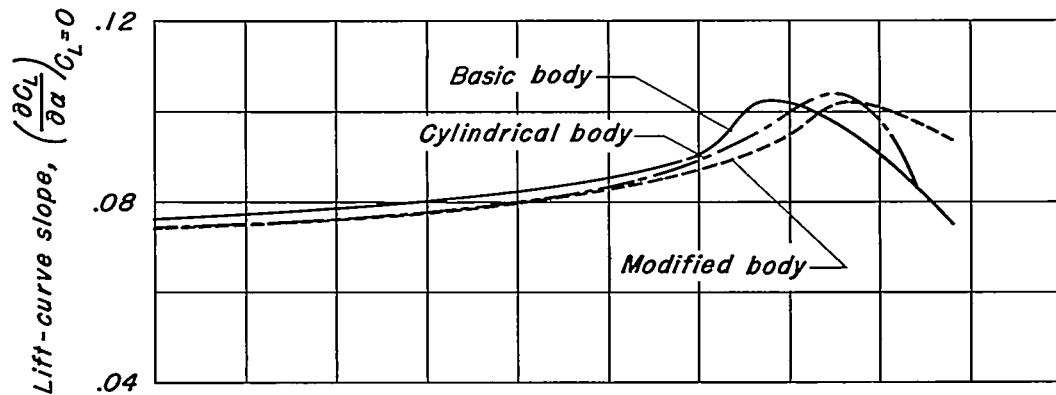


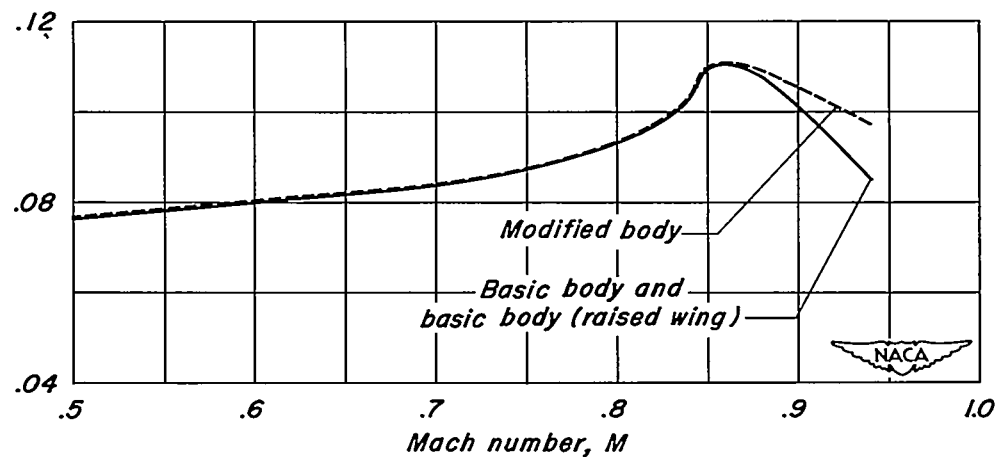
Figure 7:- Variation of drag coefficient at 0.3 lift coefficient with Mach number for the swept wing in combination with various bodies.



(a) Body with a fineness ratio of 12

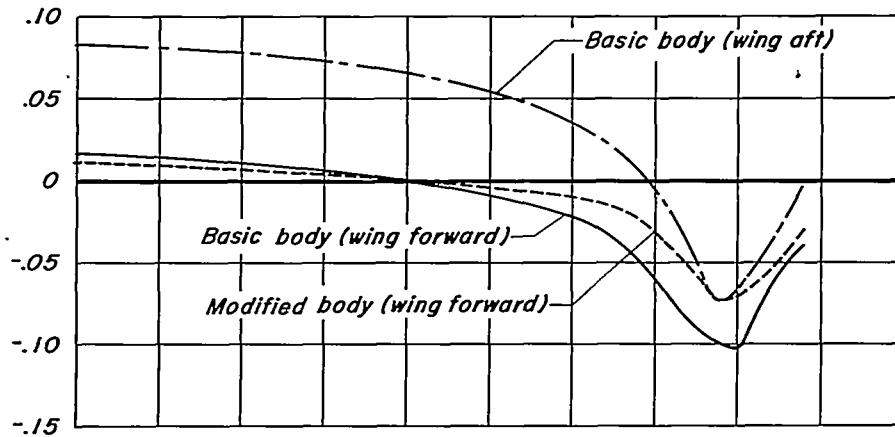


(b) Small body with a fineness ratio of 9.

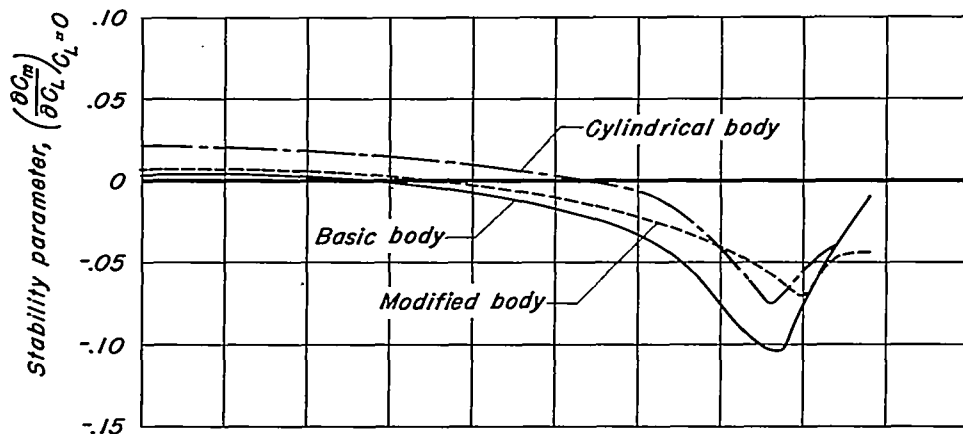


(c) Large body with a fineness ratio of 9.

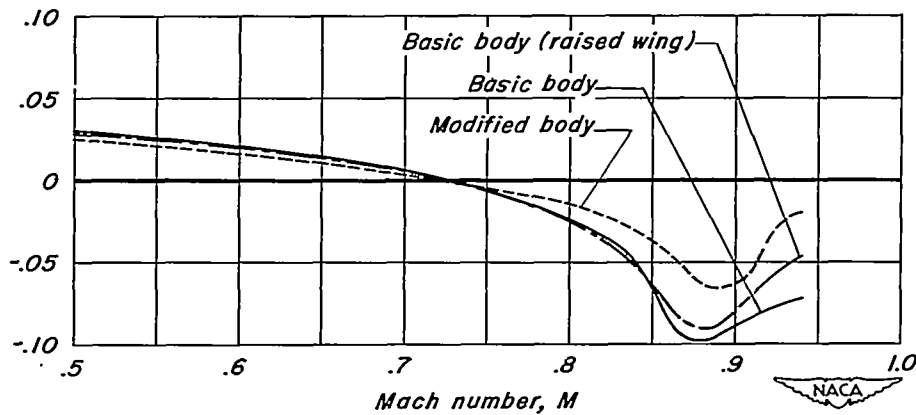
Figure 8.—Variation of lift-curve slope with Mach number for the swept wing in combination with various bodies.



(a) Body with a fineness ratio of 12

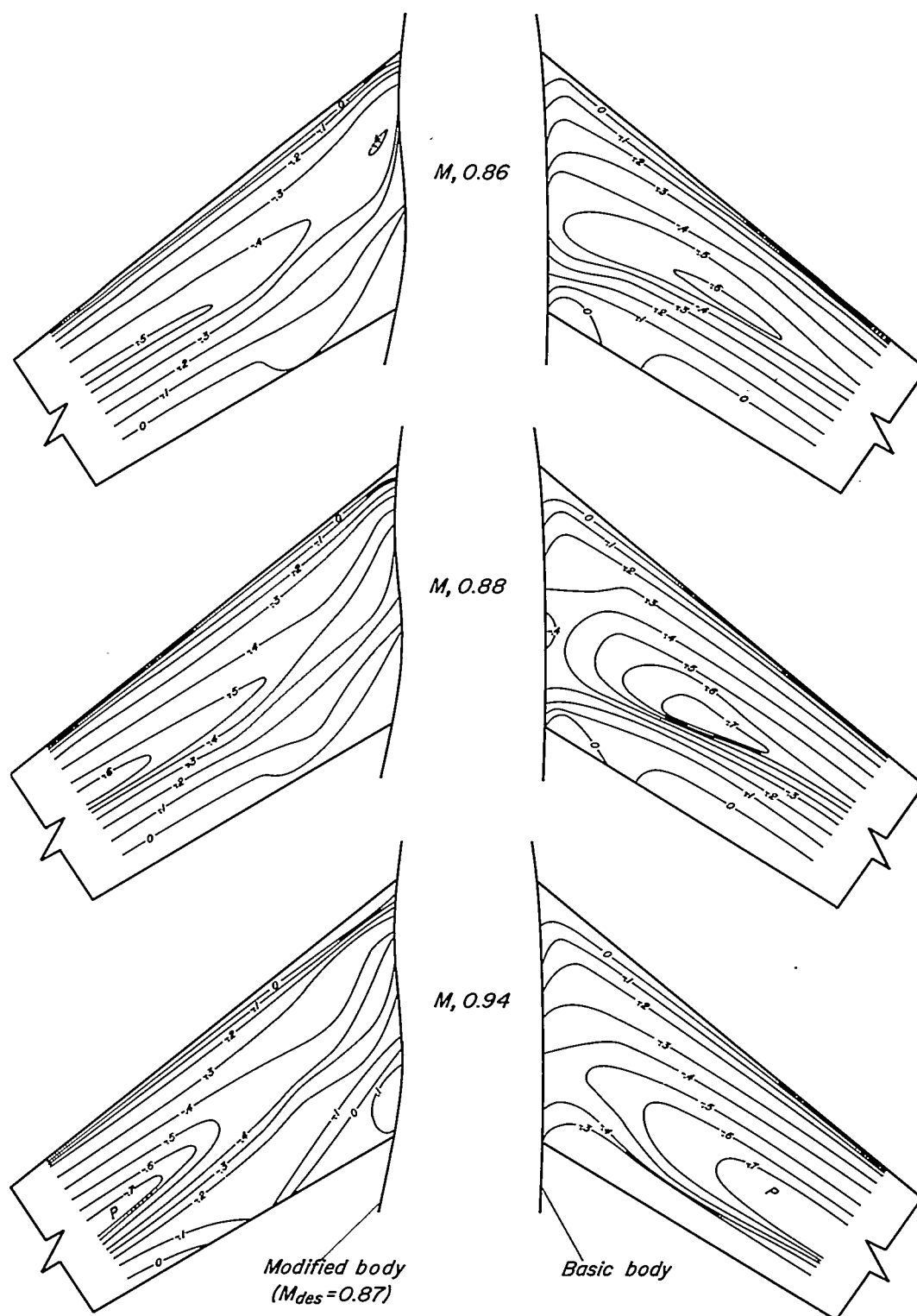



(b) Small body with a fineness ratio of 9.

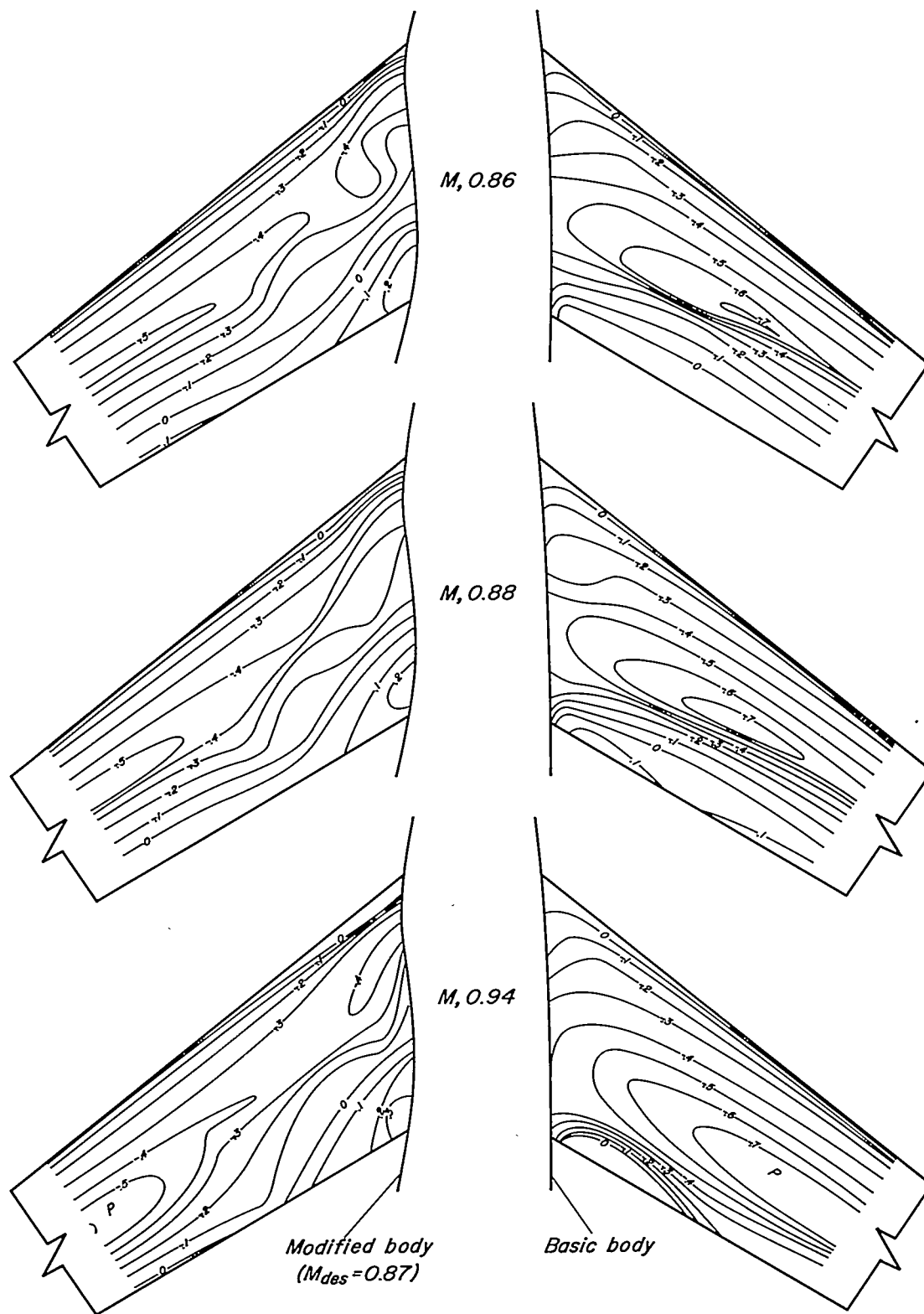


(c) Large body with a fineness ratio of 9.

Figure 9 -Variation of stability parameter $\left(\frac{\partial C_m}{\partial C_L}\right)_{C_L=0}$ with Mach number for the swept wing in combination with various bodies.



(a) Body having a fineness ratio of 12 (wing forward). 
 Figure 10.—Lines of constant pressure on the sweptback wing in combination with basic and modified bodies at zero lift.



(b) Small body having a fineness ratio of 9.
Figure 10.—Concluded.



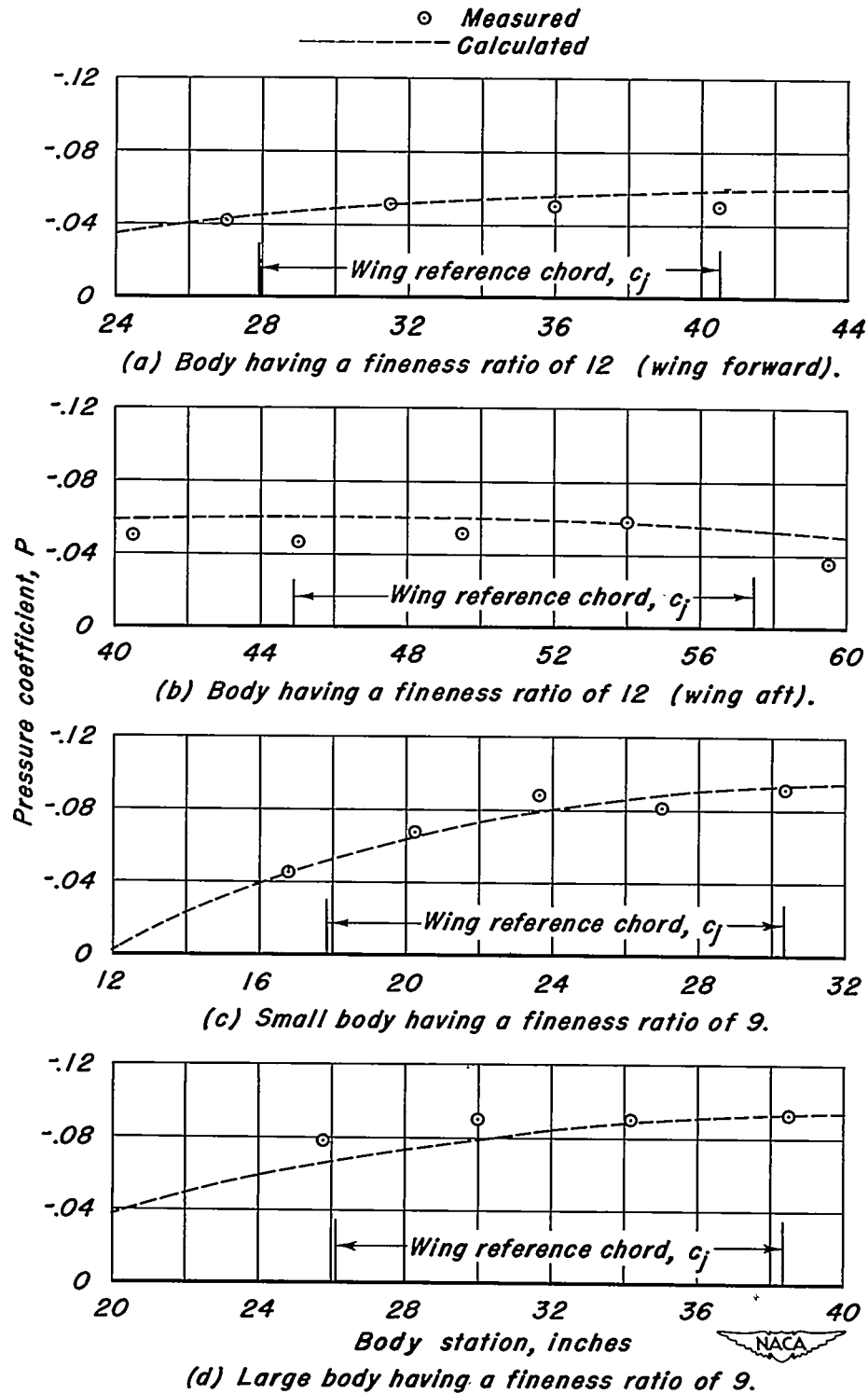


Figure 11.- Pressure distribution from body-alone tests compared with theoretical pressure distributions calculated by equation (A3) for a Mach number of 0.87.

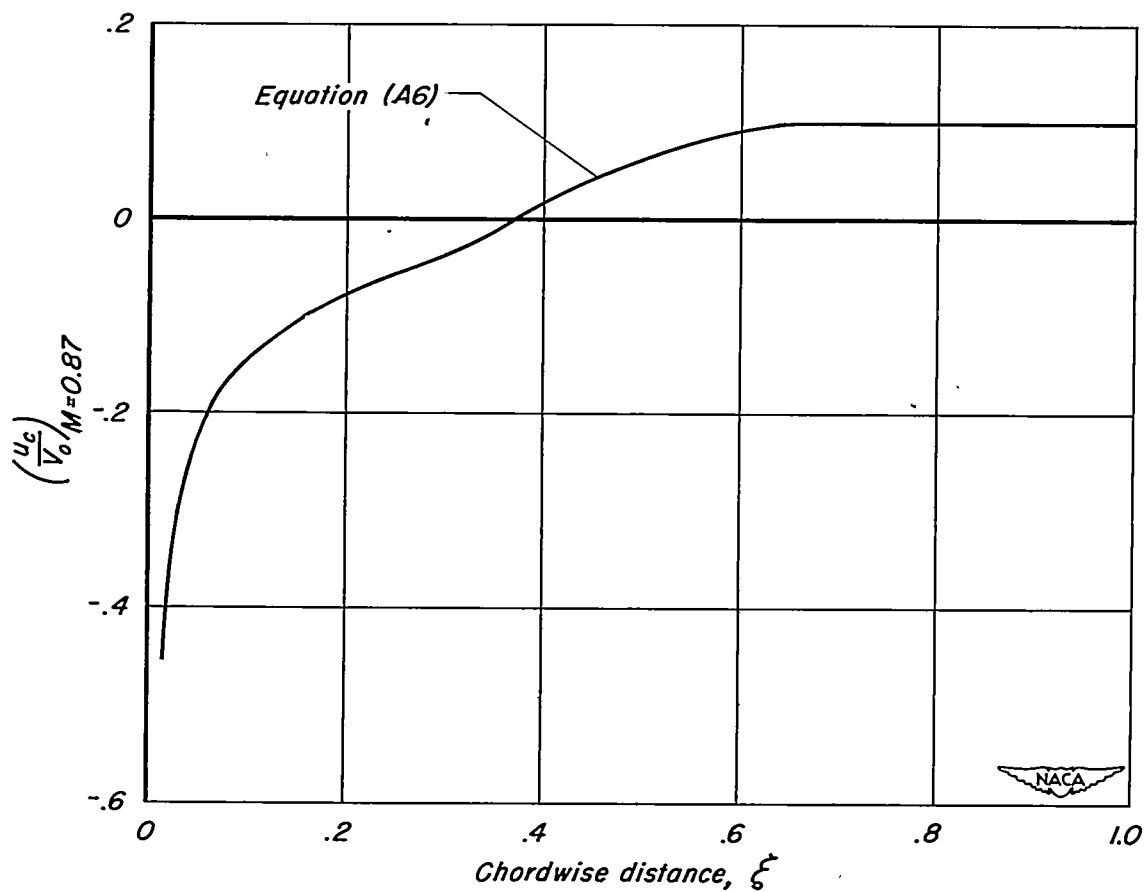


Figure 12.- Distortion velocity at the root of a 35° sweptback, untapered wing having 64₂A015 sections normal to the leading edge (Mach number of 0.87).

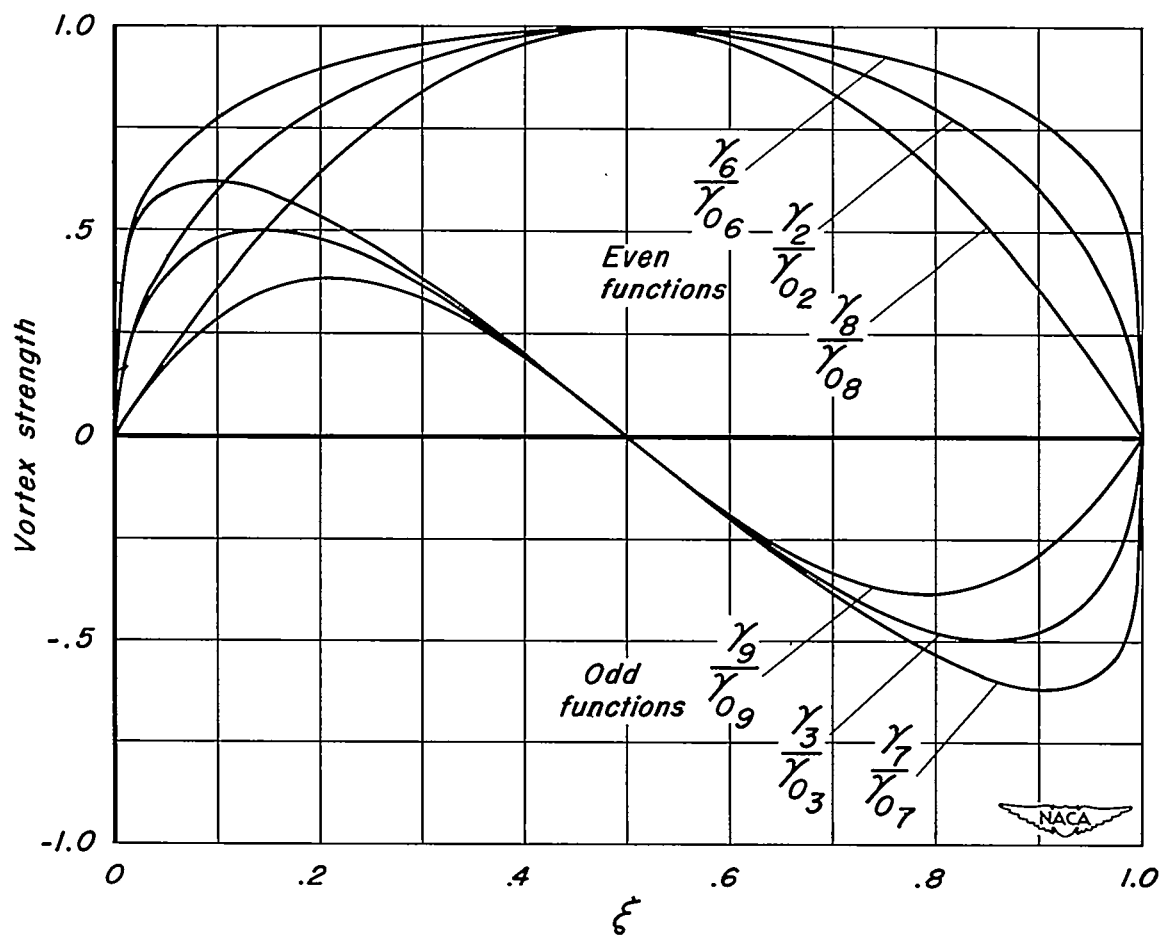
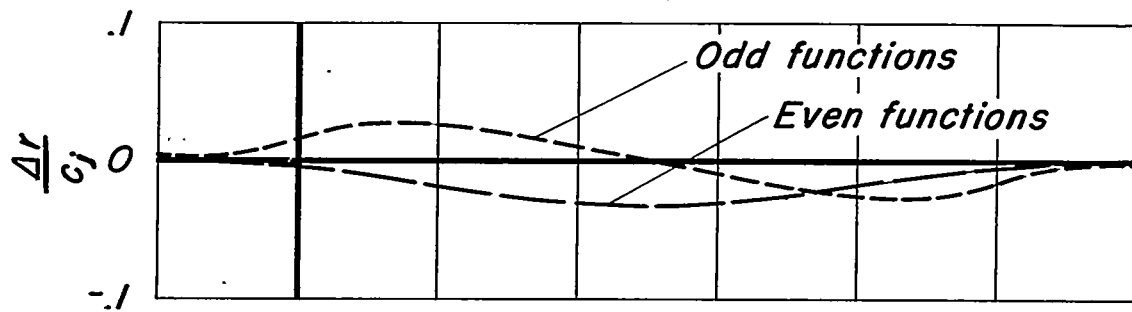
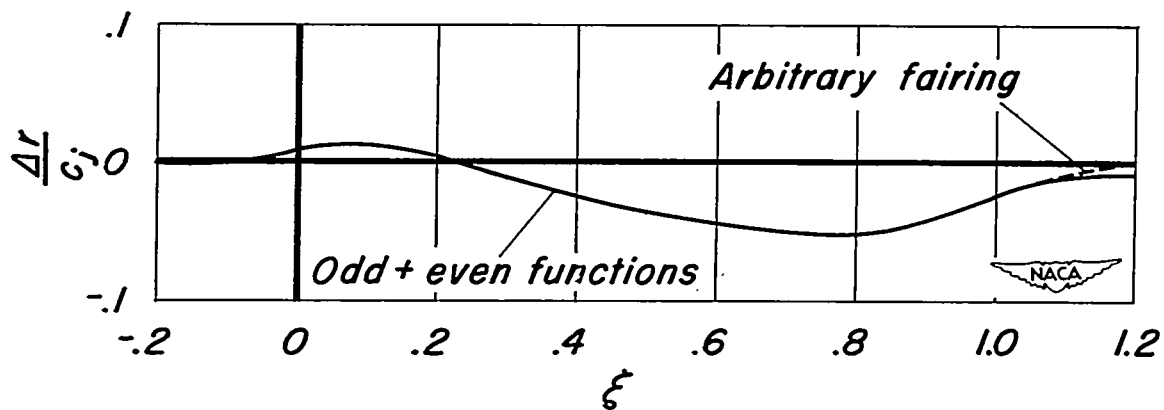


Figure 13.—Vortex distributions.



(a) Radial modification for the odd and even vortex-distribution functions.



(b) Radial modification adjusted to have zero value at $\xi = -0.2$.

Figure 14.—Radial modification as computed by the ring-vortex method for the body having a fineness ratio of 12 (wing in forward position).